

Linear control of coherent structures in wall-bounded turbulence at $Re_\tau = 2000$

Stephan F. Oehler* and Simon J. Illingworth

Department of Mechanical Engineering, The University of Melbourne, Victoria 3010, Australia

(Dated: January 12, 2023)

We consider linear feedback flow control of the largest scales in an incompressible turbulent channel flow at a friction Reynolds number of $Re_\tau = 2000$. A linear model is formed by augmenting the Navier-Stokes equations with an eddy viscosity and linearizing it about the turbulent mean. Velocity perturbations are then generated by stochastically forcing the linear operator. The objective is to reduce the kinetic energy of these velocity perturbations at the largest scales using body forces. It is shown that a control set-up with a well-placed sensor and actuator performs comparably to either measuring the flow everywhere (while actuating it at a single wall height) or actuating the flow everywhere (while measuring it at a single wall height). This idealized configuration, therefore, can provide insight into how specific scales of turbulence are most effectively measured and actuated at low computational cost.

DOI:

arXiv:1906.07462v1 [physics.flu-dyn] 18 Jun 2019

* stephan.friedrich.oehler@gmail.com

I. INTRODUCTION

A growing number of studies have successfully utilized linear models for estimation [7, 16, 29] and control [8, 22, 28] of wall-bounded turbulent flows. The work of Luhar et al. (2014) [22], in particular, suggests that linear models can qualitatively predict the effect of control on individual scales and also determine at which location they can best be measured. Linear model-based designs are an appealing alternative to direct numerical simulation (DNS) based designs since the cost is several orders of magnitude smaller. One reason for the success of linear models is that linear mechanisms play an important role in the sustenance of turbulence [19, 35]. In the linearized Navier-Stokes (LNS) equations, where the flow is linearized around the turbulent mean, these linear mechanisms result in large transient growth that is due to the non-normality of the LNS operator [37]. In particular, [9, 15, 32] showed that the LNS operator could predict the typical widths of near-wall streaks and large-scale structures in the outer layer.

Linear mechanisms play a major role in the formation and maintenance of large-scale structures in turbulent wall-bounded flows. These large-scale structures contribute significantly to the turbulent kinetic energy and Reynolds stresses (in the outer region), and there is evidence that they affect the small scales near the wall [10, 13, 24–26]. Hence, the control of these structures is crucial for any efforts to control wall-bounded flows (see Kim and Bewley 2007 [20] for a review). It was shown that linear estimation, which is closely related to linear control, performs best for those structures that have the greatest potential for transient growth [9, 32], are the most amplified in stochastically and harmonically forced settings [15] and are coherent over large wall-normal distances [23]. These observations presumably also apply to linear control, which would simplify the controller design process.

This work studies linear feedback control of the largest structures in a turbulent channel flow at a relatively high Reynolds number of $\text{Re}_\tau = 2000$. This is in part motivated by experimental work that has achieved a reduction in skin-friction drag through real-time control of large-scale structures [1]. The particular focus is on the placement of sensors and actuators for control. Specifically, we compare control performance when measuring or actuating the full channel (i.e. an ideal set-up) to control performance when measuring or actuating at only one specific wall height (which is a more realistic set-up in a practical application, e.g. hot-wire sensors and jet actuators). Consequently, it is possible to compare the ideal setting to what is achievable in a laboratory environment. Rather than testing various configurations through the use of DNS, the flow is modeled using the LNS operator for perturbations about the mean flow (§II). An eddy viscosity is included in the operator to model the effect of the incoherent scales. We introduce three specific control set-ups in §III and analyze their performance in §IV. Finally, we conclude the study in §V.

II. THE LINEAR MODEL

A statistically steady incompressible turbulent channel flow at a friction Reynolds number $\text{Re}_\tau = u_\tau h / \nu = 2000$ is considered, where ν is the kinematic viscosity, h the channel half-height, $u_\tau = \sqrt{\tau_w / \rho}$ the friction velocity, τ_w the wall shear stress, and ρ the density. Streamwise, spanwise, and wall-normal spatial coordinates are denoted by $[x, y, z]$ and the corresponding velocities by $[u, v, w]$. Spatial variables are normalized by h , wavenumbers by $1/h$, velocities by the friction velocity u_τ , time by h/u_τ and pressure p by ρu_τ^2 . This non-dimensionalization sets the channel half-height to $h = 1$ such that $z \in [0, 2h]$.

Taking the incompressible Navier-Stokes equations we form a linear operator for the perturbations $\mathbf{u} = [u, v, w]$ about the turbulent mean flow $\mathbf{U} = [U(z), 0, 0]$, where the non-linear term $\mathbf{d} = -(\mathbf{u} \cdot \nabla)\mathbf{u} + (\mathbf{u} \cdot \nabla)\mathbf{u}$ is treated as stochastic forcing, and an eddy viscosity $\nu_T(z)$ is introduced to model the effect of incoherent motions [9, 32, 33]:

$$\frac{\partial \mathbf{u}}{\partial t} = -(\mathbf{U} \cdot \nabla)\mathbf{u} - (\mathbf{u} \cdot \nabla)\mathbf{U} - \nabla p + \nabla \cdot \left[\frac{\nu_T}{\nu} (\nabla \mathbf{u} + \nabla \mathbf{u}^T) \right] + \mathbf{d}, \quad \nabla \cdot \mathbf{u} = 0. \quad (1)$$

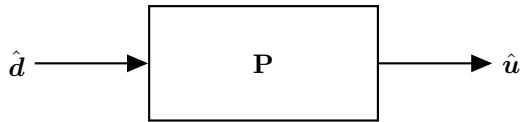
An analytical fit is used [5] for the eddy viscosity profile ν_T as in several previous studies [9, 16, 28, 32]:

$$\nu_T(z) = \frac{\nu}{2} \left\{ 1 + \frac{\kappa_1^2 \text{Re}_\tau^2}{9} (2z - z^2)^2 (3 - 4z + 2z^2)^2 \times \left[1 - \exp\left(\frac{-\text{Re}_\tau z}{\kappa_2}\right) \right]^2 \right\}^{1/2} + \frac{\nu}{2}. \quad (2)$$

Integrating $\text{Re}_\tau(1 - z)\nu/\nu_T(z)$ provides the mean velocity profile $U(z)$. The constants $\kappa_1 = 0.426$ and $\kappa_2 = 25.4$ give the best fit to the mean velocity profile of a DNS simulation at $\text{Re}_\tau = 2003$ [9, 12]. Controlling perturbations in the flow will alter the mean velocity profile and with it the linear model itself (which is formed about the mean). The controller therefore needs to be robust to account for any changes in the mean flow. It would be interesting to study robustness, but this is beyond the scope of this study.

We need to express the flow in state-space form to access standard tools from dynamics and control. To do so, we first take Fourier transforms in the homogeneous streamwise and spanwise directions to express the flow in the

Orr-Sommerfeld Squire form and then discretize in the wall-normal direction using Chebyshev collocation of order 200. (Convergence has been checked by doubling the order of the discretization.) Finally, we express the Orr-Sommerfeld Squire equations as a linear state-space model:



$$\dot{\hat{\mathbf{q}}}(t) = \mathbf{A}\hat{\mathbf{q}}(t) + \mathbf{B}\hat{\mathbf{d}}(t), \quad (3a)$$

$$\hat{\mathbf{u}}(t) = \mathbf{C}\hat{\mathbf{q}}(t), \quad (3b)$$

where $\hat{\mathbf{q}} = [\hat{\mathbf{w}}, \hat{\boldsymbol{\eta}}]^T$ represents the states of the system (wall-normal velocity and wall-normal vorticity), $\hat{\mathbf{d}} = [\hat{d}_x, \hat{d}_y, \hat{d}_z]^T$ all non-linearities and $\hat{\mathbf{u}} = [\hat{u}, \hat{v}, \hat{w}]$ the velocities ($\hat{\quad}$) denotes signals in Fourier space). We treat $\hat{\mathbf{d}}$ as stochastic forcing that is white in space and time [17]. Therefore, we account for the non-linearities by treating them as a source of intrinsic forcing to the LNS operator [27]. The matrices \mathbf{A} , \mathbf{B} , and \mathbf{C} are:

$$\mathbf{A} = \begin{bmatrix} \Delta^{-1}\mathcal{L}_{OS} & 0 \\ -ik_y U' & \mathcal{L}_{SQ} \end{bmatrix}, \quad \mathbf{B} = \begin{bmatrix} -ik_x \Delta^{-1} \mathcal{D} & -ik_y \Delta^{-1} \mathcal{D} & -k^2 \Delta^{-1} \\ ik_y & -ik_x & 0 \end{bmatrix}, \quad \mathbf{C} = \frac{1}{k^2} \begin{bmatrix} ik_x \mathcal{D} & -ik_y \\ ik_y \mathcal{D} & ik_x \\ k^2 & 0 \end{bmatrix}, \quad (4)$$

where \mathcal{L}_{OS} and \mathcal{L}_{SQ} are the Orr-Sommerfeld and Squire operators for the eddy viscosity enhanced LNS equations [4]:

$$\mathcal{L}_{OS} = ik_x(U'' - U\Delta) + \nu_T \Delta^2 + 2\nu_T' \mathcal{D}\Delta + \nu_T''(\mathcal{D}^2 + k^2), \quad (5)$$

$$\mathcal{L}_{SQ} = -ik_x U + \nu_T \Delta + \nu_T' \mathcal{D}. \quad (6)$$

Here $\mathcal{D} = \frac{\partial}{\partial z}$, $(\quad)' = \frac{\partial}{\partial z}(\quad)$, $k^2 = k_x^2 + k_y^2$, and $\Delta = \mathcal{D}^2 - k^2$. The boundary conditions are: $\hat{\mathbf{w}}_{wall}(t) = \hat{\mathbf{w}}'_{wall}(t) = \hat{\boldsymbol{\eta}}_{wall}(t) = 0$. We weight the operator \mathbf{B} with $\mathbf{M}^{-1/2}$, where \mathbf{M} is an integration matrix corresponding to Clenshaw-Curtis quadrature [36], and we choose \mathbf{C} in Eq. (3b) such that $\hat{\mathbf{u}}$ corresponds to the velocity field over one channel-half ($0 \leq z \leq h$). (See Appendix A for more information.) By taking Laplace transforms of Eq. (3) we obtain a transfer function \mathbf{P} that relates the input $\hat{\mathbf{d}}$ to the output $\hat{\mathbf{u}}$:

$$\hat{\mathbf{u}}(s) = \mathbf{P}(s)\hat{\mathbf{d}}(s), \quad (7a)$$

$$\mathbf{P}(s) = \mathbf{C}(s\mathbf{I} - \mathbf{A})^{-1}\mathbf{B}, \quad (7b)$$

where s is the Laplace variable. By setting $s = j\omega$ the frequency response (i.e. the resolvent) is obtained.

We are interested in the energy of the flow, which we quantify using the \mathcal{H}_2 -norm (Appendix C):

$$\|\hat{\mathbf{u}}\|_2 = \sqrt{\frac{1}{2\pi} \int_{-\infty}^{\infty} \text{trace}[\mathbf{P}^*(j\omega)\mathbf{M}\mathbf{P}(j\omega)] d\omega} \equiv \left[\mathbb{E} \left\{ \lim_{T \rightarrow \infty} \frac{1}{T} \int_0^T \left(\int_0^h \hat{\mathbf{u}}^*(z, t)\hat{\mathbf{u}}(z, t) dz \right) dt \right\} \right]^{1/2}, \quad (8)$$

where \mathbb{E} is the expected value and $(\quad)^*$ is the complex conjugate transpose. In the Laplace domain, the \mathcal{H}_2 -norm of $\mathbf{P}(s = j\omega)$ can be seen as the average gain between the input $\hat{\mathbf{d}}(s = j\omega)$ and the output $\hat{\mathbf{u}}(s = j\omega)$ over all frequencies and all directions.

Figure 1 shows $\|\hat{\mathbf{u}}\|_2$ for a range of k_x and k_y . We see that $\|\hat{\mathbf{u}}\|_2$ is largest at $k_x = 0$ and $k_y = 4/3$. (See Hwang and Cossu [14, 15] for a detailed analysis on the energy amplification of the laminar channel flow) In §IV.2–§IV.4, we choose to study the streamwise and spanwise wavenumber pairs that are most amplified (we select them to be $|k_x| \leq 0.5$ and $|k_y| \leq 6$, which is marked in Fig. 1).

III. THE CONTROL SET-UP

So far, we have introduced the eddy-viscosity-enhanced Orr-Sommerfeld and Squire operators that are linearized about the mean velocity profile of a turbulent channel flow. We stochastically force the linear operator to generate velocity perturbations that we now want to control. To do so, we include three new signals ($\hat{\mathbf{m}}$, $\hat{\mathbf{f}}$ and $\hat{\mathbf{z}}$) into the state-space model (Eq. 3):

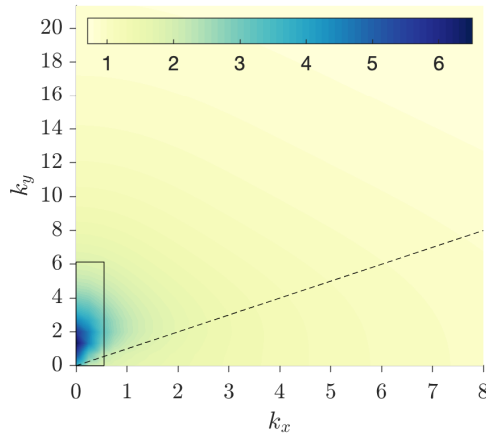


FIG. 1. The energy norm of the uncontrolled flow $\|\hat{\mathbf{u}}\|_2$ as a function of streamwise k_x and spanwise k_y wavenumber represented by fifty-nine contour levels from 0.7 (yellow) to 6.5 (blue). Also denoted on the figure are the wavenumber pairs where $k_x = k_y$ (---) and the range of wavenumbers we consider in Figs. 4, 5, 6 and 7 (□).

$$\dot{\hat{\mathbf{q}}}(t) = \mathbf{A}\hat{\mathbf{q}}(t) + \mathbf{B}\hat{\mathbf{d}}(t) + \mathbf{B}_f\hat{\mathbf{f}}(t), \quad (9a)$$

$$\dot{\hat{\mathbf{z}}}(t) = \mathbf{C}_z\hat{\mathbf{q}}(t) + \alpha\hat{\mathbf{f}}(t), \quad (9b)$$

$$\dot{\hat{\mathbf{m}}}(t) = \mathbf{C}_m\hat{\mathbf{q}}(t) + \hat{\mathbf{n}}(t). \quad (9c)$$

The first new signal $\hat{\mathbf{m}}$ represents a time-resolved velocity measurement at a single wall height ($\mathbf{C}_m\hat{\mathbf{q}}$) that is contaminated by sensor noise ($\hat{\mathbf{n}}$). We treat $\hat{\mathbf{n}}$ as an unknown forcing that is white in time with a covariance $\mathbb{E}(\hat{\mathbf{n}}\hat{\mathbf{n}}^*)$ of 10^{-4} . The second new signal $\hat{\mathbf{f}}$ represents a time-resolved body force at a single wall height to actuate the flow ($\mathbf{B}_f\hat{\mathbf{f}}$). Both $\hat{\mathbf{m}}$ and $\hat{\mathbf{f}}$ are defined in Appendix B. The third new signal $\hat{\mathbf{z}}$ (not to be confused with wall-normal variable z) represents the quantity to be minimized by control. We define $\hat{\mathbf{z}}$ to minimize the energy of the entire flow field ($\mathbf{C}_z\hat{\mathbf{q}}$) while also keeping the actuation force small ($\alpha\hat{\mathbf{f}}$, where α is a penalization on large $\hat{\mathbf{f}}$). We set the penalization to be insignificant ($\alpha = 10^{-4}$) because we want to achieve the best possible control performance. (Increasing α will gradually reduce the control performance and energy consumption of the actuator.) Minimizing the energy of the entire flow-field lets the control design process decide which perturbations to target for the best results. This is in contrast to opposition control, for example, which focuses on wall-normal velocity perturbations to eliminate streamwise streaks [22]. (See Appendix C for a derivation of the cost signal.)

III.1. The three control problems

We now want to use the system $\tilde{\mathbf{P}}$, defined in (9), to investigate three different control problems of interest. The first of these is Actuating Everywhere (AE) control, where the controller can actuate the flow everywhere but is limited to measurements at one wall height. The second is Measuring Everywhere (ME) control, where the flow is measured everywhere but now actuation is limited to one wall height. The third is Input-Output (IO) control, where sensors and actuators are limited to one wall height. This final configuration is of particular interest since it is the most feasible experimental configuration. A fourth case, where there are no limitations on which sensors or actuators are available, is not considered since it is able to instantly set the flow to the desired state. The three configurations are illustrated in Fig. 2 and the details of their state-space models can be found in Appendix C. We study AE, ME and IO because we want to know what price we have to pay when only a single actuator is available (as opposed to actuating the flow everywhere); and what price we have to pay when only a single sensor is available (as opposed to knowledge of the flow everywhere). This, in turn, provides insight on the extent to which control of the largest scales is fundamentally difficult; and on the extent to which control is limited by having only a single sensor or a single actuator.

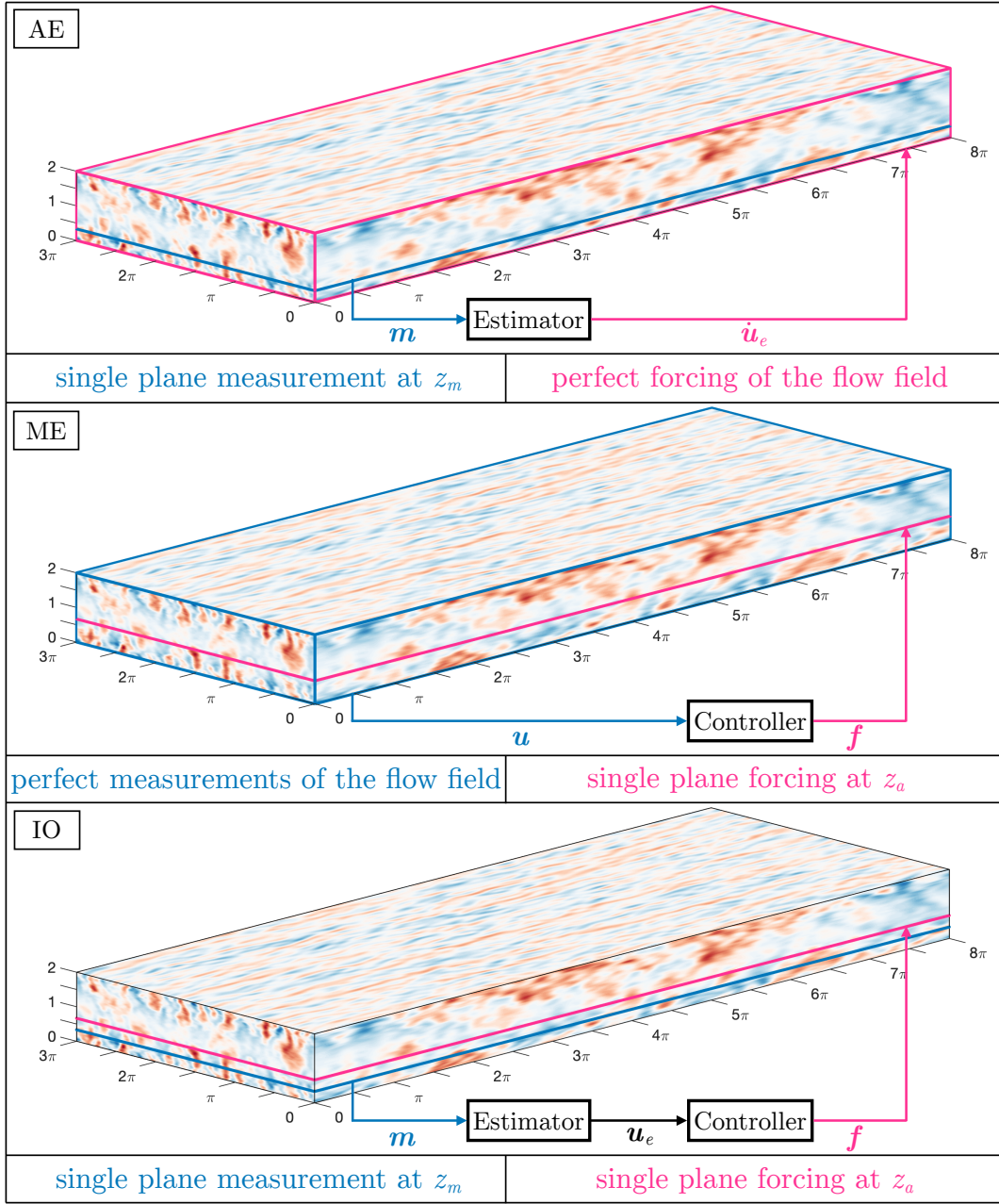


FIG. 2. The AE, ME, and IO problems.

III.1.1. Actuating Everywhere (AE) control

In the Actuating Everywhere (AE) control problem, we can actuate the flow everywhere but only have access to sensor measurements \hat{m} at a single location z_s ¹. These measurements are contaminated by sensor noise \hat{n} . The task in the AE problem is to estimate the entire state \hat{q} , and then use the estimate \hat{q}_e to control the flow. *Thus we only have one sensor to measure the flow, and we want to use it to control the flow everywhere.*

¹ It could also be multiple sensors at various locations, multiple actuators at various locations, or both.

The state estimate is generated using an estimator:

$$\dot{\hat{\mathbf{q}}}_e(t) = (\mathbf{A} - \mathbf{L}\mathbf{C}_m) \hat{\mathbf{q}}_e(t) + \mathbf{L}\hat{\mathbf{m}}(t), \quad (10a)$$

$$\hat{\mathbf{u}}_e(t) = \mathbf{C}\hat{\mathbf{q}}_e(t), \quad (10b)$$

where \mathbf{L} is the estimator gain value (designed in Appendix C). The estimator knows the dynamics of the system (represented by $\mathbf{A}\hat{\mathbf{q}}_e$), but it neither knows the initial conditions nor the stochastic disturbances $\hat{\mathbf{d}}$ that are applied to the linear operator. It corrects itself using the error between the measurement and its estimate: $\mathbf{L}(\hat{\mathbf{m}} - \mathbf{C}_m\hat{\mathbf{q}}_e)$. The estimate of the velocity field is applied as a body force to the entire flow, which immediately eliminates estimated perturbations from the flow and therefore acts as a perfect actuation set-up.

III.1.2. Measuring Everywhere (ME) control

In the Measuring Everywhere (ME) control problem, we have an actuator $\mathbf{B}_f\hat{\mathbf{f}}$ at a single location z_a^1 , and we are given knowledge of the entire system state $\hat{\mathbf{q}}$. *Thus we know everything about the flow, but we only have one actuator to control the flow.* A controller generates the actuator force $\hat{\mathbf{f}}$:

$$\hat{\mathbf{f}}(t) = -\mathbf{K}\hat{\mathbf{q}}(t), \quad (11)$$

where \mathbf{K} is the controller gain value (designed in Appendix C). The ‘measurement’ for this arrangement is the full flow field $\hat{\mathbf{q}}$, because it is assumed that the controller ‘knows everything’.

III.1.3. Input-Output (IO) control

In the Input-Output (IO) control problem, we only have one measurement $\hat{\mathbf{m}}$ at z_s available to estimate the flow, and we only have one actuator $\mathbf{B}_f\hat{\mathbf{f}}$ at z_a available to control the flow¹. The measurement $\hat{\mathbf{m}}$, which is contaminated by sensor noise $\hat{\mathbf{n}}$, is used to obtain an estimate $\hat{\mathbf{q}}_e$ (from an estimator), and the actuator force $\hat{\mathbf{f}}$ is generated with a controller that uses $\hat{\mathbf{q}}_e$. *(Thus we only have one sensor to estimate the flow, and we only have one actuator available to control the flow.)* To form a combined estimator and controller, we rewrite Eq. (11) to include $\hat{\mathbf{q}}_e$:

$$\dot{\hat{\mathbf{q}}}_e(t) = (\mathbf{A} - \mathbf{L}\mathbf{C}_m - \mathbf{B}_f\mathbf{K}) \hat{\mathbf{q}}_e(t) + \mathbf{L}\hat{\mathbf{m}}(t), \quad (12a)$$

$$\hat{\mathbf{f}}(t) = -\mathbf{K}\hat{\mathbf{q}}_e(t). \quad (12b)$$

III.2. Control performance

We quantify the magnitude of $\hat{\mathbf{z}}(s)$ with the \mathcal{H}_2 -norm for a channel half $\|\hat{\mathbf{z}}\|_2$ similar to Eq. 8 (Appendix C). From this, we define the control performance parameter $\hat{\gamma}$:

$$\hat{\gamma} = \sqrt{\frac{\|\hat{\mathbf{z}}\|_2^2}{\|\hat{\mathbf{u}}_{ref}\|_2^2}} = \sqrt{\frac{\|\hat{\mathbf{u}}_{ctrl}\|_2^2 + \alpha\|\hat{\mathbf{f}}\|_2^2}{\|\hat{\mathbf{u}}_{ref}\|_2^2}}, \quad (13)$$

where $\|\hat{\mathbf{u}}_{ref}\|_2$ is the \mathcal{H}_2 -norm of the uncontrolled reference flow, $\|\hat{\mathbf{u}}_{ctrl}\|_2$ the \mathcal{H}_2 -norm of the controlled flow, and $\|\hat{\mathbf{f}}\|_2$ the \mathcal{H}_2 -norm of the energy consumed by the actuator. The control performance parameter is defined such that $0 \leq \hat{\gamma} \leq 1$, where 0 indicates the best case scenario in which the controller eliminates all velocity perturbations, and 1 indicates the worst case scenario in which the controller achieves no reduction in the energy of the flow.

III.3. Optimal sensor and actuator placement

We want to place the sensors and actuators at the wall height that provides the best performance. To do so, we conduct an iterative minimization search across all possible sensor and actuator locations (z_s and z_a) to find the lowest $\hat{\gamma}$ possible. The iterative gradient minimization employed has been introduced and discussed in earlier studies

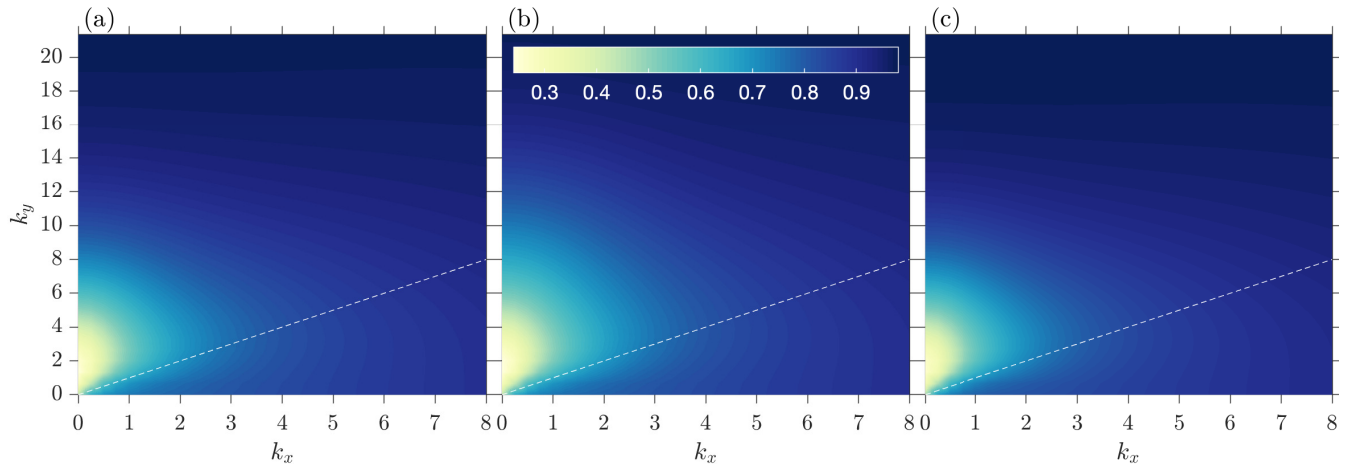


FIG. 3. The energy norms $\hat{\gamma}_{AE}$ (a), $\hat{\gamma}_{ME}$ (b) and $\hat{\gamma}_{IO}$ (c) as a function of streamwise k_x and spanwise k_y wavenumber represented by sixty-five contour levels from 0.24 (yellow) to 0.98 (blue). Also denoted on the figure are the wavenumber pairs where $k_x = k_y$ (--).

[6, 31]. By following the approach of [30] it was determined that the optimal collocated placement for the sensor and actuator is at $z_a = z_s = 0.32$. (Note that only wavenumbers satisfying $|k_x| \leq 0.5$ and $|k_y| \leq 6$ are considered while computing these optimal placement locations). We choose to collocate the sensor and actuator to simplify the problem (collocation marginally affects the performance).

IV. CONTROL PERFORMANCE

This section is in four parts: §IV.1 examines the control performance at individual wavenumber pairs; §IV.2 looks at the overall performance; §IV.3 at the performance across individual wall heights; and §IV.4 considers the energy consumed by actuation.

IV.1. Control at individual wavenumber pairs

In this section, we study the control performance of AE, ME and IO over a range of wavenumber pairs (k_x, k_y) . For this purpose, we use the parameter $\hat{\gamma}$, as defined in Eq. (13). In Fig. 3, $\hat{\gamma}$ is plotted as a function of k_x and k_y (the channel length is $x = 8\pi$ and width is $y = 3\pi$, which results in a streamwise resolution of $\Delta k_x = 1/4$ and a spanwise resolution of $\Delta k_y = 2/3$). The contours of $\hat{\gamma}$ are almost identical for the three problems. Therefore, from Fig. 3, we see that the performance of the control scenario where we have one optimally placed sensor and actuator (IO) is comparable to the cases where we actuate everywhere (AE) or know everything (ME). Hence, we observe that actuating everything does not significantly increase the control performance when we are limited to one sensor. Similarly, measuring everything does not significantly increase the control performance when we are limited to one actuator. We observe that, for all three problems, $\hat{\gamma}$ is the lowest for streamwise-constant structures ($k_x = 0$) with a spanwise wavenumber of $k_y = 4/3$. As the structures become smaller (k_x and k_y increase), $\hat{\gamma}$ increases. This behavior can partly be explained by the smaller scales being less coherent across wall-normal distances [23]. As a consequence, single sensor and actuator control at the smaller scales might not be feasible, even if we consider second-order statistics [38] or non-linear controller [21] designs.

It is important to assess whether the controllers perform well for the most energetic scales. For this, we compare Fig. 3, which shows the normalized \mathcal{H}_2 -norm for the controlled flow, with Fig. 1, which shows the \mathcal{H}_2 -norm of the uncontrolled flow. We observe that, in all the three cases, the performance of the controller is the best (low $\hat{\gamma}$) for the wavenumber pairs (k_x, k_y) that are most amplified (high $\|\hat{\mathbf{u}}\|_2$). This result is important because it shows that we can reduce the energy of the largest, most amplified scales with a limited number of sensors and actuators. The same relationship has been observed in the estimation literature [16, 23, 29]: linear estimation performs best for the wavenumber pairs (k_x, k_y) that are most amplified (high $\|\hat{\mathbf{u}}\|_2$). Therefore, the scales that we can estimate well are also those we can control well.

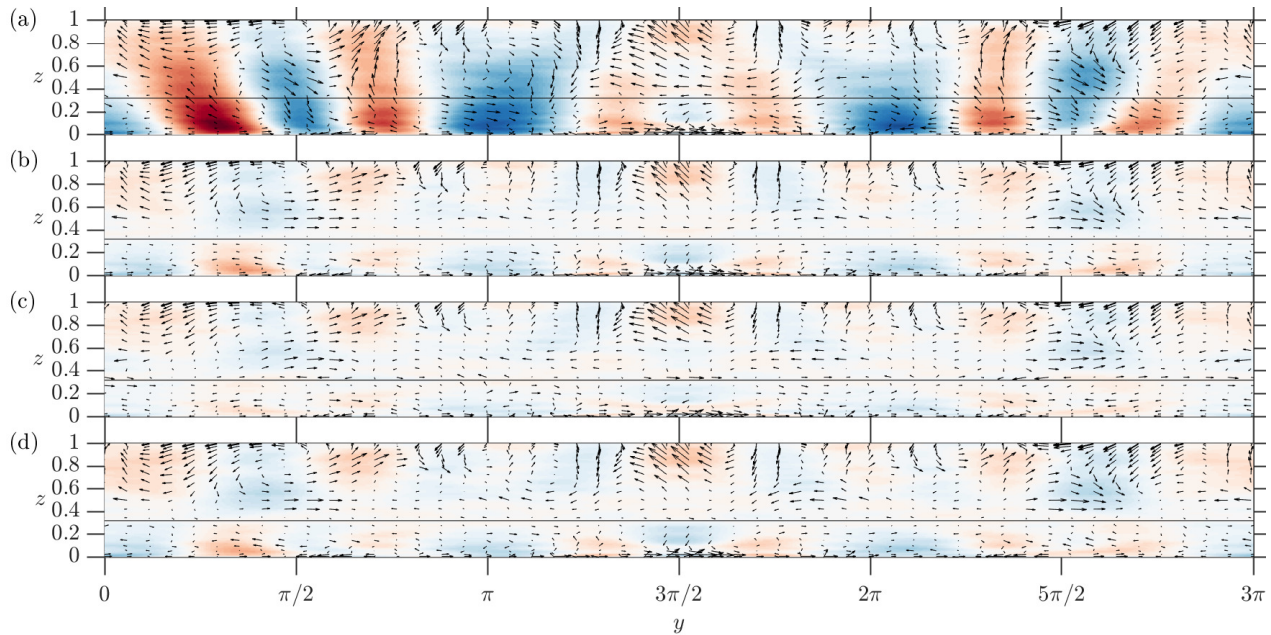


FIG. 4. Velocity perturbations (streamwise: contour; spanwise and wall-normal: vector plot) at $x = 3\pi/2$: (a) uncontrolled reference, (b) AE, (c) ME, and (d) IO. The sensor and actuator are placed at $z_s = z_a = 0.32$. Sixty-five contour levels are shown from $-|u|_{max}$ (blue) to $|u|_{max}$ (red).

γ_{AE}	γ_{ME}	γ_{IO}
0.387	0.368	0.404

TABLE I. The control performance for AE, ME and IO.

IV.2. Control in physical space

We now look at control for a set of large-scale structures: $|k_x| \leq 0.5$ and $|k_y| \leq 6$, the range of which is indicated in Fig. 1. The figure shows that these structures are the most amplified in the stochastically forced LNS model, and we can see in Fig. 3 that they are also the best for control.

We begin by looking at snapshots of the velocity perturbations in two-dimensional planes ($z - y$ at $x = 1.5\pi$) at an instance in time ($t = 0.5$, i.e. after half a channel flow-through). The data is generated from the linear model. Fig. 4a shows the flow field of the uncontrolled (reference) flow. Figs. 4b–4d show the controlled flow fields for each of the three cases AE, ME and IO, respectively. We observe that all three controllers achieve a significant reduction of the streamwise velocity perturbations everywhere. The spanwise and wall-normal velocity components are also reduced, most notably at $z_s = z_a = 0.32$ (corresponding to the location of the actuator and sensor).

It is difficult to quantify and compare the control performances from a snapshot in time. For that reason, we sum the \mathcal{H}_2 -norm across all the wavenumber pairs (k_x, k_y) considered. The parameter γ is the ratio of these summed \mathcal{H}_2 -norms computed from the controlled and the uncontrolled cases, respectively:

$$\gamma = \sqrt{\frac{\sum_{i \in k_x, j \in k_y} \|\hat{\mathbf{z}}(i, j)\|_2^2}{\sum_{i \in k_x, j \in k_y} \|\hat{\mathbf{u}}_{ref}(i, j)\|_2^2}}. \quad (14)$$

As a consequence, γ represents the normalised performance of the controller integrated across all three velocity components u , v and w . The values of γ are shown in table I, and they tell us that the overall performance is similar, although ME slightly outperforms AE and IO.

To further understand the control results, it is important to look at the impact of the controllers on each velocity component $[u, v, w]$ separately. Thus, we look at the kinetic energy (i.e. the squared \mathcal{H}_2 -norm) of each velocity

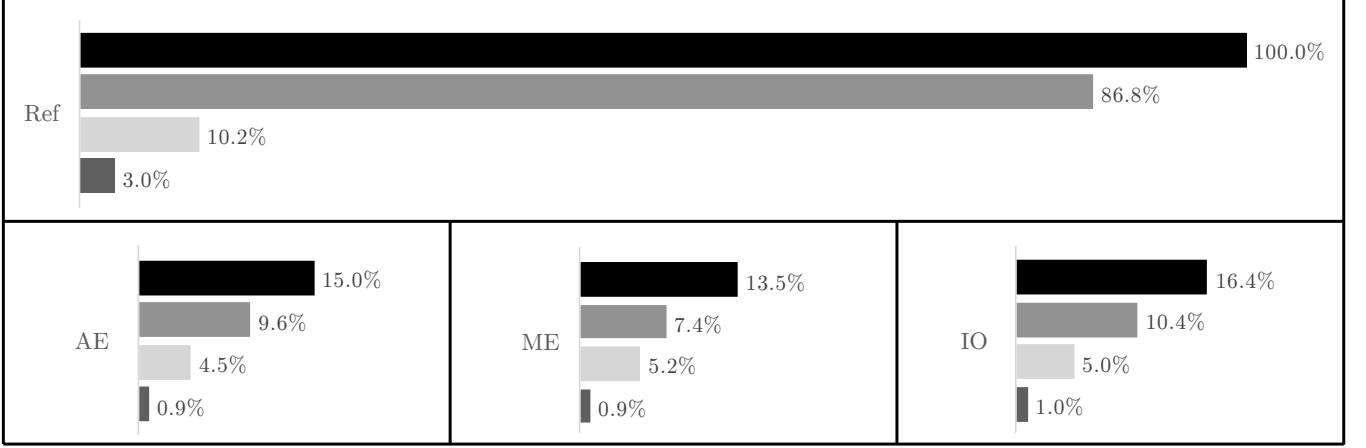


FIG. 5. The reduction of the kinetic energy relative to the entire flow: $\mathbf{E}_{u,v,w}$ (■), \mathbf{E}_u (■), \mathbf{E}_v (■) and \mathbf{E}_w (■), where $\mathbf{E}_{u,v,w} = \mathbf{E}_u + \mathbf{E}_v + \mathbf{E}_w$.

component relative to the energy of the entire uncontrolled flow-field:

$$\mathbf{E} = \frac{\sum_{i \in k_x, j \in k_y} \|\hat{\mathbf{y}}(i, j)\|_2^2}{\sum_{i \in k_x, j \in k_y} \|\hat{\mathbf{u}}_{ref}(i, j)\|_2^2}. \quad (15)$$

By setting $\hat{\mathbf{y}}$ to be different velocity components, \mathbf{E} is defined in four different ways: (i) $\mathbf{E}_{u,v,w}$, where $\hat{\mathbf{y}}$ represents all the three velocity components, (ii) \mathbf{E}_u where $\hat{\mathbf{y}}$ represents the streamwise velocity component, (iii) \mathbf{E}_v , where $\hat{\mathbf{y}}$ represents the spanwise velocity component, and (iv) \mathbf{E}_w , where $\hat{\mathbf{y}}$ represents the wall-normal velocity component. Figure 5 shows \mathbf{E} for the uncontrolled reference flow (denoted as Ref) and for the flow subject to AE, ME and IO. In the reference flow, the majority of the energy is contained in u (87%) and the remaining energy in v (10%) and w (3%). After we apply control, we see that, consistent with figs. 3 and 4 and table I, the performances of AE, ME and IO are all similar to each other. The overall reduction of energy ($\mathbf{E}_{u,v,w}$) is $\approx 85\%$, where \mathbf{E}_u is reduced by $\approx 90\%$, \mathbf{E}_v by $\approx 50\%$ and \mathbf{E}_w by $\approx 67\%$. Therefore, the control system is most effective in reducing the streamwise velocity component, which also carries most of the energy.

IV.3. Control across wall heights

So far, we have looked at the control performance over an entire channel half. It is also important to study the performance of the controllers across wall heights.

For reference, we first compute the normalized kinetic energy of the uncontrolled flow \mathbf{E}_z as a function of wall-normal location z :

$$\mathbf{E}_z(z) = \frac{\sum_{i \in k_x, j \in k_y} \|\hat{\mathbf{y}}_{ref}(i, j, z)\|_2^2}{\max(\sum_{i \in k_x, j \in k_y} \|\hat{\mathbf{y}}_{ref}(u, j, z)\|_2^2)}. \quad (16)$$

Figure 6 shows \mathbf{E}_z as a function of z on the right axis. As in the previous section, the signal $\hat{\mathbf{y}}$ represents: all the three velocity components (Fig. 6a), the streamwise velocity component (Fig. 6b), the spanwise velocity component (Fig. 6c), or the wall-normal velocity component (Fig. 6d). From the plot of \mathbf{E}_z (in blue), we observe that u and v are strongest near the wall (Figs. 6b and 6c), while w is strongest near the channel center (Fig. 6d).

We now look at the reduction in the kinetic energy of the controlled flow ϵ as a function of wall-normal location z :

$$\epsilon(z) = 1 - \frac{\sum_{i \in k_x, j \in k_y} \|\hat{\mathbf{y}}_{ctrl}(i, j, z)\|_2^2}{\sum_{i \in k_x, j \in k_y} \|\hat{\mathbf{y}}_{ref}(i, j, z)\|_2^2}. \quad (17)$$

There are four different definitions of ϵ (depending on $\hat{\mathbf{y}}$), which are shown in Figs. 6a-6d on the left axis. As before, $\hat{\mathbf{y}}$ represents either all three (Fig. 6a) or individual (Fig. 6b-d) velocity components. Parameter ϵ is shown for AE

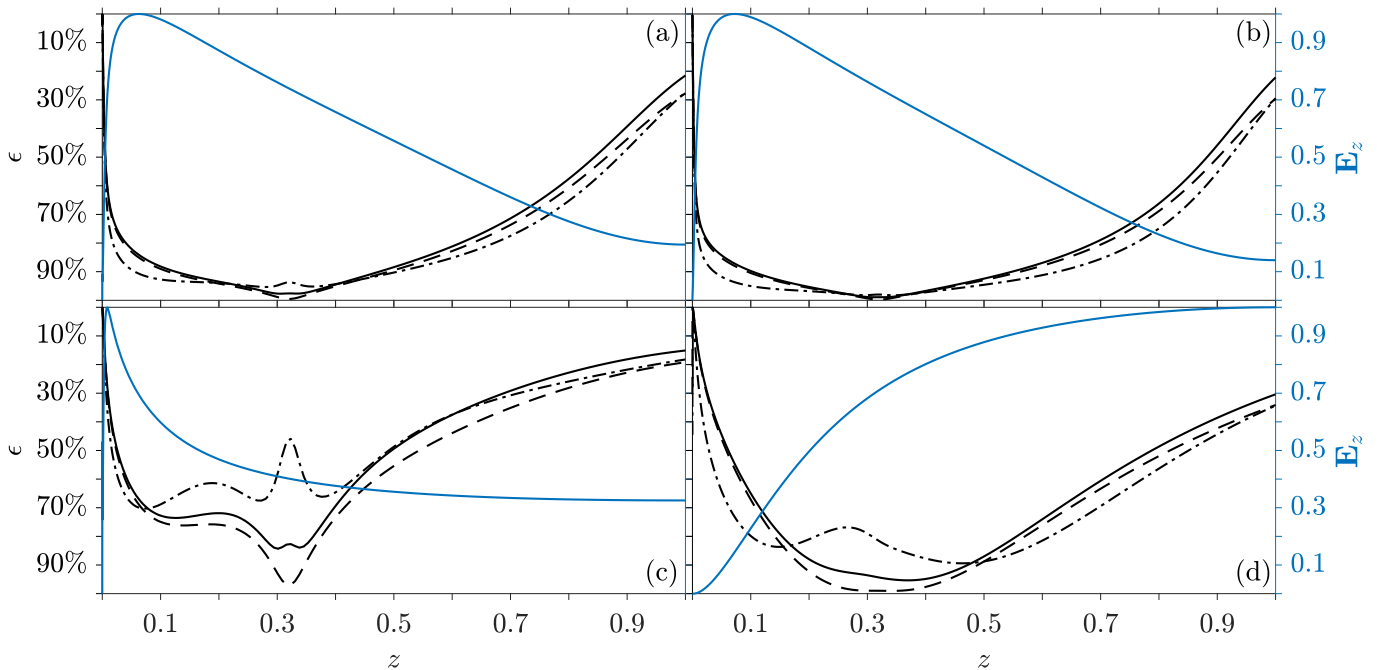


FIG. 6. Left axis: The reduction of kinetic energy (ϵ_{AE} (--), ϵ_{ME} (- · -) and ϵ_{IO} (—)) as a function of z . Right axis: the normalized kinetic energy \mathbf{E}_z (—) as a function of z . Results are shown for (a) $[u, v, w]$, (b) $[u]$, (c) $[v]$ and (d) $[w]$.

(ϵ_{AE}), ME (ϵ_{ME}), and IO (ϵ_{IO}). By definition, ϵ is between $0 \leq \epsilon \leq 1$, where 1 (100%) indicates the elimination of all kinetic energy and 0 (0%) indicates that there is no reduction in kinetic energy.

From Fig. 6a we observe that the performance for all control problems is best near $z_s = z_a = 0.32$ (where $\epsilon(z)$ is lowest) and decreases with distance from it. A significant reduction of velocity perturbations is observed at all wall heights. Similar values of ϵ are achieved in Fig. 6b for the streamwise velocity component, which can be explained by u being the most energetic component (Fig. 5). AE and IO set v in Fig. 6c close to zero around $z_s = z_a = 0.32$. While ME also reduced the energy carried by v , the reduction is not as strong as in the case of AE and IO. Figure 6d shows that all three problems set the wall-normal velocity close to zero at one wall height. The transport of momentum in the vicinity of this wall height is attenuated, which prevents the formation of streamwise structures [34]. This mechanism is employed in opposition-controlled wall-bounded flows [11], where the controller is specifically designed to create a plane of zero wall-normal momentum that is referred to as a “virtual wall”. We did not choose an opposition control design but instead selected a general cost function to reduce velocity perturbations everywhere. Since the three \mathcal{H}_2 -optimal control designs seem to all create a “virtual wall”, the results suggest that this approach is the most effective one in the control of turbulent channel flows utilizing single-plane sensors and single-plane actuators.

Let us compare ϵ_{ME} , where the flow field is known everywhere, to ϵ_{IO} , where only one location is known. We see that ME performs marginally better than IO everywhere outside the vicinity of the sensor at $z = 0.32$. This suggests that IO is focusing its control efforts on the region near $z = 0.32$ (that it ‘knows well’) at the expense of a slight reduction in control performance everywhere else. If we compare ϵ_{AE} , where actuation is provided everywhere, to ϵ_{IO} , where actuation is provided at only one location, we can see that they are almost identical to each other except in the vicinity of the actuator at $z = 0.32$. Therefore, near $z = 0.32$, the performance of IO must be primarily limited by the single actuator; while at all other locations its performance is limited by the single sensor.

IV.4. Control forces

So far, we have studied the effect that the three control problems have on the velocity perturbations. Each problem continuously forces the flow to prevent perturbations from growing. In this section, we study these continuous forces. In particular, we look at the percentage of the forcing that is applied to the streamwise, spanwise and wall-normal directions. For this purpose, in Fig. 7, we plot the energy consumed by f_x , f_y and f_z as a percentage of the total \mathbf{f} ,

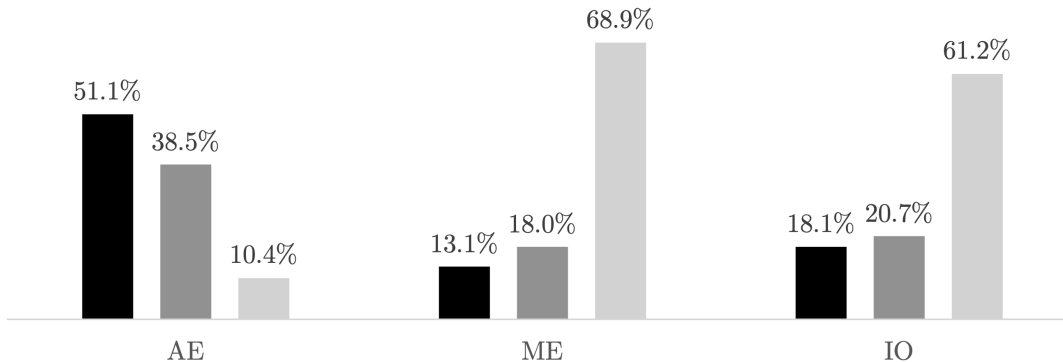


FIG. 7. The distribution of forcing between \mathbf{E}_{f_x} (■), \mathbf{E}_{f_y} (▣) and \mathbf{E}_{f_z} (▨), where $\mathbf{E}_{f_x} + \mathbf{E}_{f_y} + \mathbf{E}_{f_z} = 1$

which we refer to as \mathbf{E}_{f_x} , \mathbf{E}_{f_y} and \mathbf{E}_{f_z} (see Appendix C for the \mathcal{H}_2 -norms):

$$\mathbf{E}_f = \frac{\sum_{i \in k_x, j \in k_y} \|\hat{f}(i, j)\|_2^2}{\sum_{i \in k_x, j \in k_y} \|\hat{f}(i, j)\|_2^2}. \quad (18)$$

We observe that in AE, which actuates the flow everywhere, the largest forcing component is \mathbf{E}_{f_x} (streamwise) and the smallest forcing component is \mathbf{E}_{f_z} (wall-normal). In ME and IO, which actuate the flow at only one location, the largest forcing component is \mathbf{E}_{f_z} (wall-normal) and the smallest forcing component is \mathbf{E}_{f_x} (streamwise). We can explain these results using two mechanisms:

- (i) Direct elimination: velocity perturbations are counter-perturbed as soon as they are detected, which is mostly employed by AE. One may ask why AE only allocates $\mathbf{E}_{f_x} \approx 51\%$ of energy to f_x even though the energy reduction in the streamwise direction is responsible for $\approx 91\%$ of the overall energy reduction. The answer is that, once we apply control, streamwise perturbations are not given a chance to amplify, which allows the controller to allocate more energy to f_y and f_z .
- (ii) Indirect elimination: is used for wall heights at which actuation is not available. As soon as velocity perturbations are detected, the actuator introduces counter-perturbations in the wall-normal direction, thus leveraging shear to eliminate the large-scale streamwise streaks. The indirect elimination technique is employed by ME and IO, and explains their high allocation of energy to f_z ($\mathbf{E}_{f_z} = 68.9\%$ in ME and $\mathbf{E}_{f_z} = 61.2\%$ in IO). The streamwise f_x and spanwise f_y forces primarily affect control locally around the actuator location and as a consequence are given less priority.

V. CONCLUSIONS

We have considered linear feedback control of a turbulent channel at $\text{Re}_\tau = 2000$ using the linearized Navier-Stokes equations (LNS). The linear operator is augmented with an eddy viscosity (following many previous studies) and is assumed to be stochastically forced. The LNS equation was employed because it provides insight into control, without the requirement of running costly DNS or experimental studies. The particular focus was on three control problems: (i) AE, where measurements are limited to one optimal wall height, but actuation is available everywhere; (ii) ME, where actuators are limited to one optimal wall height, but measurements are available everywhere; and (iii) IO, where sensors and actuators are limited to one optimal wall height. All three problems performed similarly. From these results we can infer that measuring everywhere does not significantly increase the control performance when we are limited to one actuator location. Likewise, actuating everywhere does not significantly increase the control performance when we are limited to one sensor location. Our three control problems perform best for the largest scales that (i) are high in energy when stochastically forced, (ii) exhibit large transient growth and (iii) are coherent over large wall-normal distances. Therefore, we choose to look at a specific range of wavenumbers ($|k_x| \leq 0.5$ and $|k_y| \leq 6$), corresponding to the largest scales, in more detail. We saw an overall reduction in kinetic energy of $\approx 85\%$, where the streamwise velocity component was most attenuated (by $\approx 90\%$). To further analyze the largest scales, we looked at the effect of control at individual wall heights. The performance was best near the sensor and actuator location ($z = 0.32$) and deteriorated with distance from it. Finally, we looked at the distribution of the forcing between the

streamwise f_x , spanwise f_y and wall-normal f_z components. For AE, f_x was strongest and f_z weakest, while for ME and IO, f_z was strongest and f_x weakest. AE, which forces the flow everywhere, relies on directly eliminating structures as soon as they are detected, which is why it prioritizes streamwise forcing f_x . Meanwhile ME and IO, which only force the flow at a single location, mainly employ wall-normal forcing (f_z), thereby eliminating velocity perturbations by leveraging the mean wall-normal shear.

ACKNOWLEDGMENTS

The authors would like to thank Sean Symon and Anagha Madhusudanan for their extensive feedback and support during the creation of this paper and are grateful for the financial support of the Australian Research Council.

Appendix A: Spectral discretisation of the channel equation

We generate the eddy viscosity profile and mean velocity profile (Eq. (2)) for one channel half using Chebyshev collocation of order $N_\nu = 200$ [36]. Barycentric Lagrange interpolation [3] is used to map the results to both channel halves. For the main channel flow (Eq. (3)) we employ Chebyshev collocation of order $N_c = 200$. When looking at results for a single channel half, we employ barycentric interpolation to map the outputs onto a Chebyshev grid of order $N_{out} = 200$. We apply stochastic forcing, which is white in space and time, at each grid point i with a covariance $\mathbb{E}(\hat{d}_i \hat{d}_i^*) = 1$, where \mathbb{E} the expected value. Integration is implemented with the Clenshaw-Curtis quadrature [36], which provides weights w_i at each Chebyshev point and is used to form the integration matrix: $\mathbf{M} = \text{diag}([w_1, w_2, \dots, w_i, \dots, w_N])$.

Appendix B: Sensor and actuator matrices

The measurement signal is defined as:

$$\hat{\mathbf{m}} = \mathbf{C}_y \hat{\mathbf{u}} + \hat{\mathbf{n}} = \mathbf{C}_y \mathbf{C} \hat{\mathbf{q}} + \hat{\mathbf{n}} = \mathbf{C}_m \hat{\mathbf{q}} + \hat{\mathbf{n}}, \quad (\text{B1})$$

where $\hat{\mathbf{n}}$ is the sensor noise and \mathbf{C}_y represents the sensor matrix. We treat $\hat{\mathbf{n}}$ as an unknown forcing that is white in time, and we set the covariance $\mathbb{E}(\hat{\mathbf{n}} \hat{\mathbf{n}}^*) = (10^{-4}) \mathbf{I} = \mathbf{V}^{1/2}$ such that the sensor noise is negligible but the system is well-posed. The sensor matrix \mathbf{C}_y is defined as:

$$\mathbf{C}_y = \begin{bmatrix} \mathbf{g}(z_s) & 0 & 0 \\ 0 & \mathbf{g}(z_s) & 0 \\ 0 & 0 & \mathbf{g}(z_s) \end{bmatrix}, \quad (\text{B2})$$

where

$$\mathbf{g}(z_s) = \exp \left\{ - \left(\frac{z - z_s}{2\sigma_s} \right)^2 \right\}^T \mathbf{M} \quad (\text{B3})$$

is a Gaussian function, $z = [z_1, z_2 \dots z_{N_{out}+1}]^T$ are Chebyshev grid points, z_s is the sensor location and σ_s defines the width of the Gaussian. We set $\sigma_s = 0.02$, which is sufficiently wide for the sensor to be independent of the output-grid resolution.

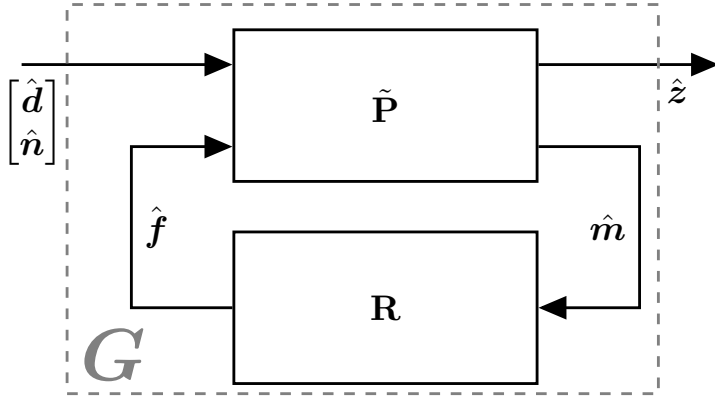
The actuator force is $\hat{\mathbf{f}}$, and it is applied at a single wall-normal location (z_a) via the matrix \mathbf{B}_f (Eq. (9a)):

$$\mathbf{B}_f \hat{\mathbf{f}} = \mathbf{B} \begin{bmatrix} \mathbf{h}(z_a) & 0 & 0 \\ 0 & \mathbf{h}(z_a) & 0 \\ 0 & 0 & \mathbf{h}(z_a) \end{bmatrix} \begin{bmatrix} \hat{f}_x \\ \hat{f}_y \\ \hat{f}_z \end{bmatrix}, \quad (\text{B4})$$

where

$$\mathbf{h}(z_a) = \exp \left\{ - \left(\frac{z - z_a}{2\sigma_a} \right)^2 \right\} \quad (\text{B5})$$

is a Gaussian function, $z = [z_1, z_2 \dots z_{N_c+1}]^T$ are Chebyshev grid points and σ_a defines the width of the Gaussian. We set $\sigma_a = 0.02$, which is sufficiently wide to be independent of the system-grid resolution.

FIG. 8. Block diagram of \mathbf{G} .

$\begin{array}{c} \text{flow } f \\ \text{input} \\ \text{flow } m \\ \text{output} \end{array}$	$\begin{array}{c} \text{single plane} \\ \text{forcing} \\ \text{at } z_a \end{array}$	$\begin{array}{c} \text{perfect} \\ \text{forcing of} \\ \text{the flow field} \end{array}$
$\begin{array}{c} \text{single plane} \\ \text{measurement} \\ \text{at } z_s \end{array}$	IO	AE
$\begin{array}{c} \text{perfect} \\ \text{measurements} \\ \text{of the flow field} \end{array}$	ME	not considered

FIG. 9. Inputs and outputs of the control problems.

Appendix C: Control

1. Control objective

The control objective \hat{z} (Eq. (9b)) is derived from the following cost function that is used for \mathcal{H}_2 -optimal control problems:

$$J = \mathbb{E} \left\{ \lim_{T \rightarrow \infty} \frac{1}{T} \int_0^T \left(\int_0^h |\hat{u}(z, t)|^2 dz + \alpha^2 |\hat{f}(t)|^2 \right) dt \right\}, \quad (\text{C1})$$

where

$$\int_0^h |\hat{u}(z, t)|^2 dz + \alpha^2 |\hat{f}(t)|^2 \equiv [\mathbf{M}^{1/2} \mathbf{C} \hat{q}(t)]^* [\mathbf{M}^{1/2} \mathbf{C} \hat{q}(t)] + [\alpha \hat{f}(t)]^* [\alpha \hat{f}(t)] = [\hat{z}(t)]^* [\hat{z}(t)]. \quad (\text{C2})$$

2. The estimator and controller gain matrices

The gain matrix \mathbf{L} for AE is designed by solving the following Ricatti equation:

$$\mathbf{A}\mathbf{Y} + \mathbf{Y}\mathbf{A}^* - \mathbf{Y}\mathbf{C}_y^* \mathbf{V}^{-1} \mathbf{C}_y \mathbf{Y} + \mathbf{B}_d \mathbf{B}_d^* = 0, \quad (\text{C3a})$$

$$\mathbf{L} = \mathbf{Y}\mathbf{C}_y^* \mathbf{V}^{-1}. \quad (\text{C3b})$$

The gain matrix \mathbf{K} for ME is designed by solving the following Ricatti equation:

$$\mathbf{A}^* \mathbf{X} + \mathbf{X}\mathbf{A} - \mathbf{X}\mathbf{B}_f \mathbf{R}^{-1} \mathbf{B}_f^* \mathbf{X} + \mathbf{C}_z^* \mathbf{C}_z = 0, \quad (\text{C4a})$$

$$\mathbf{K} = \mathbf{R}^{-1} \mathbf{B}_f^* \mathbf{X}, \quad (\text{C4b})$$

where $\mathbf{R} = \alpha^2 \mathbf{I}$. The principle of separation for estimation and control states that the independently designed \mathbf{L} and \mathbf{K} are still optimal when combined [18]. Therefore, we do not have to find them again for IO.

3. State-space model

The AE, ME and IO problems introduce a secondary system \mathbf{R} to the flow $\tilde{\mathbf{P}}$ (Fig. 8), where \mathbf{R} is either an estimator, a controller or both (Fig. 2). To quantify the control performance of the three problems, we need to express the feedback interconnection of $\tilde{\mathbf{P}}$ and \mathbf{R} as a single transfer function.

The measurement signal \hat{m} acts as an input and the force signal \hat{f} as an output to the secondary system:

$$\hat{f}(t) = \mathbf{R}(t) \hat{m}(t). \quad (\text{C5})$$

The signals $\hat{\mathbf{m}}$ and $\hat{\mathbf{f}}$ depend on the problem we consider (Fig. 9). By substituting $\mathbf{R}\hat{\mathbf{m}}$ for $\hat{\mathbf{f}}$ in $\tilde{\mathbf{P}}$ (Eq. (9)), we can form the overall state-space model \mathbf{G} (Fig. 8), using a linear fractional transformation (LFT) [2]:



where $\mathbf{A}_L \hat{\mathbf{x}}$ describes the state dynamics, $\mathbf{B}_L \hat{\mathbf{w}}$ the input dynamics and $\mathbf{C}_L \hat{\mathbf{x}}$ the output dynamics of the LFT.

To form the LFT for AE we ignore $\hat{\mathbf{f}}$ in $\tilde{\mathbf{P}}$ (Eq. (9)) and directly apply $\hat{\mathbf{q}}_e$ (Eq. (10b)) to $\hat{\mathbf{q}}$. The state-space model of $\mathbf{G}_{AE}(t)$ is:

$$\dot{\hat{\mathbf{q}}} = (\mathbf{A} - \mathbf{L}\mathbf{C}_m) \hat{\mathbf{q}} + [\mathbf{B}_d \quad -\mathbf{L}\mathbf{V}^{1/2}] \begin{bmatrix} \hat{\mathbf{d}} \\ \hat{\mathbf{n}} \end{bmatrix}, \quad (\text{C7})$$

$$\hat{\mathbf{z}} = \mathbf{C}_z \hat{\mathbf{q}}. \quad (\text{C8})$$

To form the LFT for ME we ignore $\hat{\mathbf{m}}$ in $\tilde{\mathbf{P}}$ (Eq. (9)) and directly form $\hat{\mathbf{f}}$ from $\hat{\mathbf{q}}$ (Eq. (11)). The state-space model of \mathbf{G}_{ME} is:

$$\begin{aligned} \dot{\hat{\mathbf{q}}} &= (\mathbf{A} - \mathbf{B}_f \mathbf{K}) \hat{\mathbf{q}} + \mathbf{B}_d \hat{\mathbf{d}}, \\ \hat{\mathbf{z}} &= \begin{bmatrix} \mathbf{C}_z \\ -\mathbf{R}^{1/2} \mathbf{K} \end{bmatrix} \hat{\mathbf{q}}. \end{aligned}$$

To form the LFT for IO we combine \mathbf{R} (Eq. (12)) with $\tilde{\mathbf{P}}$ (Eq. (9)). The state-space model of \mathbf{G}_{IO} is:

$$\begin{aligned} \begin{bmatrix} \dot{\hat{\mathbf{q}}} \\ \dot{\hat{\mathbf{q}}}_e \end{bmatrix} &= \begin{bmatrix} \mathbf{A} & -\mathbf{B}_f \mathbf{F} \\ \mathbf{L}\mathbf{C}_m & \mathbf{A} - \mathbf{B}_f \mathbf{F} - \mathbf{L}\mathbf{C}_m \end{bmatrix} \begin{bmatrix} \hat{\mathbf{q}} \\ \hat{\mathbf{q}}_e \end{bmatrix} + \begin{bmatrix} \mathbf{B}_d & \mathbf{0} \\ \mathbf{0} & \mathbf{L}\mathbf{V}^{1/2} \end{bmatrix} \begin{bmatrix} \hat{\mathbf{d}} \\ \hat{\mathbf{n}} \end{bmatrix}, \\ \hat{\mathbf{z}} &= \begin{bmatrix} \mathbf{C}_z & \mathbf{0} \\ \mathbf{0} & -\mathbf{R}^{1/2} \mathbf{K} \end{bmatrix} \begin{bmatrix} \hat{\mathbf{q}} \\ \hat{\mathbf{q}}_e \end{bmatrix}. \end{aligned}$$

4. \mathcal{H}_2 -norms: Uncontrolled flow

The \mathcal{H}_2 -norm for one channel half is

$$\|\hat{\mathbf{u}}\|_2 = \sqrt{\text{tr}(\mathbf{C}_z \mathbf{Z} \mathbf{C}_z^*)}, \quad (\text{C9})$$

and at individual heights it is

$$\|\hat{\mathbf{u}}(z)\|_2 = \sqrt{\text{diag}(\mathbf{C}\mathbf{Z}\mathbf{C}^*)}, \quad (\text{C10})$$

where \mathbf{Z} is found by solving the following Lyapunov equation:

$$\mathbf{A}\mathbf{Z} + \mathbf{Z}\mathbf{A}^* = -\mathbf{B}\mathbf{B}^*. \quad (\text{C11})$$

5. \mathcal{H}_2 -norms: Controlled flow

The \mathcal{H}_2 -norms for one channel half are

$$\|\hat{\mathbf{z}}_{AE}\|_2 = \sqrt{\text{tr}(\mathbf{C}_z \mathbf{Y} \mathbf{C}_z^*)}, \quad (\text{C12})$$

$$\|\hat{\mathbf{z}}_{ME}\|_2 = \sqrt{\text{tr}(\mathbf{B}_d^* \mathbf{X} \mathbf{B}_d)}, \quad (\text{C13})$$

$$\|\hat{\mathbf{z}}_{IO}\|_2 = \sqrt{\text{tr}(\mathbf{C}_z \mathbf{Y} \mathbf{C}_z^*) + \text{tr}(\mathbf{C}_m \mathbf{Y} \mathbf{X} \mathbf{L})} = \sqrt{\text{tr}(\mathbf{B}_w^* \mathbf{X} \mathbf{B}_w) + \text{tr}(\mathbf{K} \mathbf{Y} \mathbf{X} \mathbf{B}_f)}. \quad (\text{C14})$$

The \mathcal{H}_2 -norms at individual wall heights are

$$\|\hat{\mathbf{z}}_{AE}(z)\|_2 = \sqrt{\text{diag}(\mathbf{C}\mathbf{W}_c\mathbf{C}^*)} = \sqrt{\text{diag}(\mathbf{C}\mathbf{Y}\mathbf{C}^*)}, \quad (\text{C15})$$

$$\|\hat{\mathbf{z}}_{ME}(z)\|_2 = \sqrt{\text{diag}\left(\begin{bmatrix} \mathbf{C} \\ \mathbf{0} \end{bmatrix} \mathbf{W}_c \begin{bmatrix} \mathbf{C} \\ \mathbf{0} \end{bmatrix}^*\right)}, \quad (\text{C16})$$

$$\|\hat{\mathbf{z}}_{IO}(z)\|_2 = \sqrt{\text{diag}\left(\begin{bmatrix} \mathbf{C} & \mathbf{0} \\ \mathbf{0} & \mathbf{0} \end{bmatrix} \mathbf{W}_c \begin{bmatrix} \mathbf{C} & \mathbf{0} \\ \mathbf{0} & \mathbf{0} \end{bmatrix}^*\right)}, \quad (\text{C17})$$

where \mathbf{W}_c is the controllability Gramian that is found by solving the following Lyapunov equation (based on the LFT):

$$\mathbf{A}_L \mathbf{W}_c + \mathbf{W}_c \mathbf{A}_L^* = -\mathbf{B}_L \mathbf{B}_L^*. \quad (\text{C18})$$

6. \mathcal{H}_2 -norms: Actuation force

The \mathcal{H}_2 -norms for the actuator forces are

$$\|\hat{\mathbf{f}}_{AE}\|_2 = \sqrt{\text{tr}((\mathbf{C}_z \mathbf{L} \mathbf{C}_m) \mathbf{W}_c (\mathbf{C}_z \mathbf{L} \mathbf{C}_m)^*)} = \sqrt{\text{tr}((\mathbf{C}_z \mathbf{L} \mathbf{C}_m) \mathbf{Y} (\mathbf{C}_z \mathbf{L} \mathbf{C}_m)^*)}, \quad (\text{C19})$$

$$\|\hat{\mathbf{f}}_{ME}(z)\|_2 = \sqrt{\text{tr}\left(\begin{bmatrix} \mathbf{0} \\ \mathbf{R}^{1/2} \mathbf{K} \end{bmatrix} \mathbf{W}_c \begin{bmatrix} \mathbf{0} \\ \mathbf{R}^{1/2} \mathbf{K} \end{bmatrix}^*\right)}, \quad (\text{C20})$$

$$\|\hat{\mathbf{f}}_{IO}(z)\|_2 = \sqrt{\text{tr}\left(\begin{bmatrix} \mathbf{0} & \mathbf{0} \\ \mathbf{0} & \mathbf{R}^{1/2} \mathbf{K} \end{bmatrix} \mathbf{W}_c \begin{bmatrix} \mathbf{0} & \mathbf{0} \\ \mathbf{0} & \mathbf{R}^{1/2} \mathbf{K} \end{bmatrix}^*\right)}. \quad (\text{C21})$$

-
- [1] M. R. Abbassi, W. J. Baars, N. Hutchins, and I. Marusic. Skin-friction drag reduction in a high-Reynolds-number turbulent boundary layer via real-time control of large-scale structures. *Int. J. Heat Fluid Flow*, 67:30–41, 2017.
- [2] K. J. Aström and R. M. Murray. *Feedback systems: an introduction for scientists and engineers*. Princeton University Press, 2010.
- [3] J. P. Berrut and L. N. Trefethen. Barycentric Lagrange Interpolation. *SIAM Rev.*, 46(3):501–517, 2004.
- [4] R. Betchov and W. O. Criminale. Spatial instability of the inviscid jet and wake. *Phys. Fluids*, 9(2):359–362, 1966.
- [5] R. D. Cess. *A survey of the literature on heat transfer in turbulent tube flow*. Westinghouse Research, 1958.
- [6] K. K. Chen and C. W. Rowley. H_2 optimal actuator and sensor placement in the linearised complex Ginzburg-Landau system. *J. Fluid Mech.*, 681:241–260, 2011.
- [7] M. Chevalier, J. Hoepffner, T. R. Bewley, and D. S. Henningson. State estimation in wall-bounded flow systems. Part 2. Turbulent flows. *J. Fluid Mech.*, 552:167–187, 2006.
- [8] L. Cortelezzi, J. L. Speyer, K. H. Lee, and J. Kim. Robust reduced-order control of turbulent channel flows via distributed sensors and actuators. In *Proc. 37th IEEE Conf. Decis. Control*, volume 2, pages 1906–1911. IEEE, 1998.
- [9] J. C. del Alamo and J. Jiménez. Linear energy amplification in turbulent channels. *J. Fluid Mech.*, 559:205–213, 2006.
- [10] S. Duvvuri and B. J. McKeon. Triadic scale interactions in a turbulent boundary layer. *J. Fluid Mech.*, 767, R4, 2015.
- [11] E. P. Hammond, T. R. Bewley, and P. Moin. Observed mechanisms for turbulence attenuation and enhancement in opposition-controlled wall-bounded flows. *Phys of Fluids*, 10(9):2421–2423, 1998.
- [12] S. Hoyas and J. Jiménez. Scaling of the velocity fluctuations in turbulent channels up to $\text{Re}_\tau = 2003$. *Phys. Fluids*, 18(1):1–4, 2006.
- [13] N. Hutchins and I. Marusic. Large-scale influences in near-wall turbulence. *Philos. Trans. Royal Soc. A*, 365(1852):647–664, 2007.
- [14] Y. Hwang and C. Cossu. Amplification of coherent streaks in the turbulent Couette flow: an input–output analysis at low Reynolds number. *J. Fluid Mech.*, 643:333–348, 2010.
- [15] Y. Hwang and C. Cossu. Linear non-normal energy amplification of harmonic and stochastic forcing in the turbulent channel flow. *J. Fluid Mech.*, 664:51–73, 2010.
- [16] S. J. Illingworth, J. P. Monty, and I. Marusic. Estimating large-scale structures in wall turbulence using linear models. *J. Fluid Mech.*, 842:146–162, 2018.
- [17] M. R. Jovanović and B. Bamieh. Componentwise energy amplification in channel flows. *J. Fluid Mech.*, 534:145–183, 2005.
- [18] R. E. Kalman. Contributions to the theory of optimal control. *Bol. soc. mat. mexicana*, 5(2):102–119, 1960.

- [19] J. Kim. Physics and control of wall turbulence for drag reduction. *Philos. Trans. Royal Soc. A*, 369(1940):1396–1411, 2011.
- [20] J. Kim and T. R. Bewley. A linear systems approach to flow control. *Annu. Rev. Fluid Mech.*, 39(1):383–417, 2007.
- [21] E. Lauga and T. R. Bewley. Performance of a linear robust control strategy on a nonlinear model of spatially developing flows. *J. Fluid Mech.*, 512:343–374, 2004.
- [22] M. Luhar, A. S. Sharma, and B. J. McKeon. Opposition control within the resolvent analysis framework. *J. Fluid Mech.*, 749:597–626, 2014.
- [23] A. Madhusudanan, S. J. Illingworth, and I. Marusic. Coherent large-scale structures from the linearized Navier-Stokes equations. *J. Fluid Mech.*, In press:19, 2019.
- [24] I. Marusic, R. Mathis, and N. Hutchins. High Reynolds number effects in wall turbulence. *Int. J. Heat Fluid Fl.*, 3(31):418–428, 2010.
- [25] I. Marusic, R. Mathis, and N. Hutchins. Predictive model for wall-bounded turbulent flow. *Science*, 329(5988):193–196, 2010.
- [26] R. Mathis, N. Hutchins, and I. Marusic. Large-scale amplitude modulation of the small-scale structures in turbulent boundary layers. *J. Fluid Mech.*, 628:311–337, 2009.
- [27] B. J. McKeon and A. S. Sharma. A critical-layer framework for turbulent pipe flow. *J. Fluid Mech.*, 658:336–382, 2010.
- [28] R. Moarref and M. R. Jovanović. Model-based design of transverse wall oscillations for turbulent drag reduction. *J. Fluid Mech.*, 707:205–240, 2012.
- [29] S. Oehler, A. Garcia-Gutiérrez, and S. Illingworth. Linear estimation of coherent structures in wall-bounded turbulence at $Re_\tau = 2000$. *J. Phys. Conf. Ser.*, 1001:012006, 2018.
- [30] S. F. Oehler and S. J. Illingworth. Linear estimation and control of coherent structures in wall-bounded turbulence at $Re_\tau = 2000$. In *21st Australasian Fluid Mechanics Conference*. AFMS, 2018.
- [31] S. F. Oehler and S. J. Illingworth. Sensor and actuator placement trade-offs for a linear model of spatially developing flows. *J. Fluid Mech.*, 854:34–55, 2018.
- [32] G. Pujals, M. García-Villalba, C. Cossu, and S. Depardon. A note on optimal transient growth in turbulent channel flows. *Phys. Fluids*, 21(1):015109, 2009.
- [33] W. C. Reynolds and A. K. M. F. Hussain. The mechanics of an organized wave in turbulent shear flow. Part 3. Theoretical models and comparisons with experiments. *J. Fluid Mech.*, 54:263–288, 1972.
- [34] T. Sadayoshi and I. Tomoaki. Interaction between a large-scale structure and near-wall structures in channel flow. *J. Fluid Mech.*, 524:249–262, 2005.
- [35] W. Schoppa and F. Hussain. Coherent structure generation in near-wall turbulence. *J. of Fluid Mech.*, 453:57–108, 2002.
- [36] L. N. Trefethen. *Spectral methods in MATLAB*. Society for Industrial and Applied Mathematics, 2000.
- [37] L. N. Trefethen, A. E. Trefethen, S. C. Reddy, and T. A. Driscoll. Hydrodynamic stability without eigenvalues. *Science*, 261(5121):578–584, 1993.
- [38] A. Zare, M. R. Jovanović, and T. T. Georgiou. Colour of turbulence. *J. Fluid Mech.*, 812:636–680, 2017.